IEEE Access
Multidisciplinary | Rapid Review | Open Access Journal

Received March 2, 2021, accepted March 15, 2021, date of publication April 1, 2021, date of current version April 13, 2021.

Digital Object Identifier 10.1109/ACCESS.2021.3070381

Experimental Comparison of Optical Inline 3D Measurement and Inspection Systems

LUKAS TRAXLER, LAURIN GINNER, SIMON BREUSS, AND BERNHARD BLASCHITZ
Center for Vision, Automation & Control – High-Performance Vision Systems, AIT Austrian Institute of Technology, 1210 Vienna, Austria
Corresponding author: Lukas Traxler (lukas.traxler@ait.ac.at)

ABSTRACT Fast optical 3D inline inspection sensors are a powerful tool to advance factory automation. Many of these visual inspection tasks require high speeds, high resolutions, and repeatability. Stereo vision, photometric stereo, light sectioning, and structured light are the most common principles for inline imaging in the several micrometers to sub-millimeter resolution range. Selecting the correct sensor principle can be challenging as manufacturers' datasheets frequently use different values to describe their systems and do not stick to proposed characterizations defined by the "Initiative Fair Data Sheet" or the VDE/VDI standards. With the help of standardized parameters, this paper aims to compare four different measurement principles, namely AIT's own single sensor light field camera method, a structured light pattern projector, a laser triangulation sensor, and a stereo camera system, with an approximate field of view of 100×100mm. We demonstrate simple yet meaningful experiments to determine lateral resolution, temporal noise, and calibration accuracy to enable an objective system comparison. Additionally, the reproduction of small surface structures and an overall performance on a challenging test object is evaluated. Results show that the measurement principles partly serve different application areas. The provided methods will help end users to select the correct sensor for specific applications.

INDEX TERMS Automatic optical inspection, optical imaging, measurement accuracy, measurement precision, visual inspection, inline imaging, 3D imaging.

I. INTRODUCTION

To assist inspection tasks, vision systems are a crucial part in many manufacturing and quality control processes. Production demands challenging requirements on the optical inspection system, namely high throughput, detection of small defects, both glossy and dark inspection surfaces, and precise 3D height measurements of moving objects [1]–[3]. There are a huge number of optical 3D imaging methods, which generally differ in speed and quality depending on environmental conditions [4], [5]. The pros and cons of different metrology methods are often difficult to grasp by the user. Technical terms are frequently used differently when comparing product data sheets. This problem is addressed by the "Initiative Fair Data Sheet" [6] (http://www.optassyst.de/fairesdatenblatt/) supported by numerous partners from research and industry. Furthermore, acquisition techniques strongly differ in their robustness to different object types, surrounding illumination conditions, and environmental conditions found in industrial applications.

The associate editor coordinating the review of this manuscript and approving it for publication was Chao Zuo.

A. INLINE INSPECTION SYSTEMS – CURRENT STATE OF THE ART

Optical 3D imaging modalities greatly differ in their resolution, depth range, and acquisition speed. In this paper we focus on inline 3D inspection tasks with a Field of View (FOV) of approximately >100 mm and a lateral sampling of around 50 μm/pixel, which are capable of being used in inline processes, and hence for inspection of objects moving across the FOV. In this realm one finds industrial inspection sensors based on systems having an active structured light projection or passive stereo camera systems [2], [7]–[9]. The following sections introduce the different approaches, their physical limitations, and pros and cons specific to each approach.

1) STRUCTURED LIGHT

The family of structured light or active illumination techniques is based on the principle that a spatially defined intensity pattern is projected onto the inspection surface,

while a camera observes this surface. If the surface is planar, the acquired image is similar to the projected structure. Any deviation gives information on the 3D surface topology [10].

Structured light techniques can be categorized into two groups: those that apply static pattern projectors (one shot) or dynamic pattern projectors (multi-shot) [10]. Static light patterns can fail due to discontinuous object topology [7]. To overcome this problem light codes can be used: Multiple light patters are projected in temporal succession, which allows for an absolute 3D depth reading. The measurement suffers from inaccurate geometric parameters, mechanical, and thermal stability, optical surface properties, and volumetric scattering [7]. One multi-shot approach is the **fringe pattern projection** [11], which is chosen as a candidate in the comparison for this paper; the **"PhoXi XS" by Photoneo** is evaluated as a representative for this category.

Pattern projectors can be applied to moving objects [12], but for objects in motion **laser line triangulation** is often the tool of choice [13]–[15]. Its major advantage is that the camera sensor only has to capture a single object plane along the illuminated light sheet. By using a Scheimpflug configuration, the depth range and acquisition volume can be much larger than other systems [16], [17]. Errors in laser line triangulation can be induced by surface roughness properties, laser line intensity fluctuations, inhomogeneous surface textures, surface slope, and volume scattering (e.g. plastics) [7]. All monochromatic laser based systems cannot capture color texture images directly which can be a disadvantage e.g. for defects which are only visible in the surface (color) texture but not in the 3D topology, further coherent illuminations often suffer from speckle, which ultimately limits the achievable accuracy [18]. The **"LJ-X8400" by Keyence** was chosen as a device for this category.

For accurate measurements a proper system calibration is required. The calibration comprises two parts: a) a typical camera calibration [19], [20] and b) a geometric calibration of the pattern projection. The latter can be seen as an inverse camera calibration. It can be established by observing the projection onto a plane with a calibrated camera, thus the projector-calibration (b) depends on the accuracy of the camera calibration (a) [10], [21], [22]. For the special case of laser line triangulation, an extensive review was published by Xu *et al.* [23].

2) MULTIVIEW STEREO SYSTEMS

Multi View Stereo (MVS) systems comprise another family of inspection methods which do not rely on spatially defined illumination, but on the perspective observation from two or more viewing angles. Compared to structured illumination systems, its benefits are a higher robustness against ambient light [24], the systems inherently produce (color) texture images, and a reduced system complexity as no dedicated projectors are needed. The relatively simple configuration of **stereo camera systems** can be extended by additional cameras, hence additional viewing angles (MVS), to better handle occlusion problems. For fast inline inspections dual line-scan cameras are typically used [26], [27]. The largest drawback compared to active illumination systems is the required presence of texture information for stereoscopic feature matching, objects with insufficient texture are inherently difficult to acquire. As an example for an inline line-scan passive stereo scanner the **"3DPIXA dual 30um" by Chromasens** was tested.

The Calibration for a stereo camera system follows a standard camera calibration model for each camera [27], [28].

To maximize the robustness against occlusions, and to be able to inspect dark and glossy objects, we developed an inline Light Field (LF) acquisition setup and computational imaging algorithms, called Inline Computational Imaging (ICI) [29]: the algorithms combine depth information from the LF and the orientation of surface normals obtained by applying Photometric Stereo (PS)-algorithms to images from different illumination directions [30], [31]; applied calibration procedures and compensation for transport artifacts allow precise measurements [32], [33]. Additionally, it could be shown that the technology can be scaled to optical resolutions in the μm and sub-μm range [34]. Recently the algorithms have been adapted to suit the acquisition process of high-speed area cameras [35], [36]. Our **"ICI"**-system is the fourth system we benchmarked in the comparison in this paper. As it is subject of ongoing research [36], the current status is described in a separate section.

B. CONTRIBUTION AND AIM OF THIS PAPER

The aim of this paper is to benchmark the performance of the novel ICI-system, which combines LF and information from different illumination directions. The system is tested together with other typical inline inspection systems, which use different acquisition approaches.

Furthermore, the paper presents generalized empirical methods for a quantitative assessment of 3D imaging systems in consistence with the ''Initiative Fair Data Sheet''. These methods allow for a simple evaluation of the system's measurement resolution, the calibration accuracy across the full acquisition volume, and roughness measurements of metallic surfaces, which were performed using a standard surface roughness target according to ISO 25178 / DIN EN ISO 4287 [37].

For qualitative assessment, a challenging reference scene including glossy, dark, and detailed structures is acquired with all systems. Different analyses reveal advantages and disadvantages of various acquisition types.

This paper's contribution can be summarized as follows:

- introduction of a novel ICI-system utilizing 4 light directions
- presenting useful methods for experimental system assessment in accordance with present standards
- objective performance comparison of commercial inline inspection systems based on the ''Initiative Fair Data Sheet'' namely:
  - AIT ICI, an inline LF camera

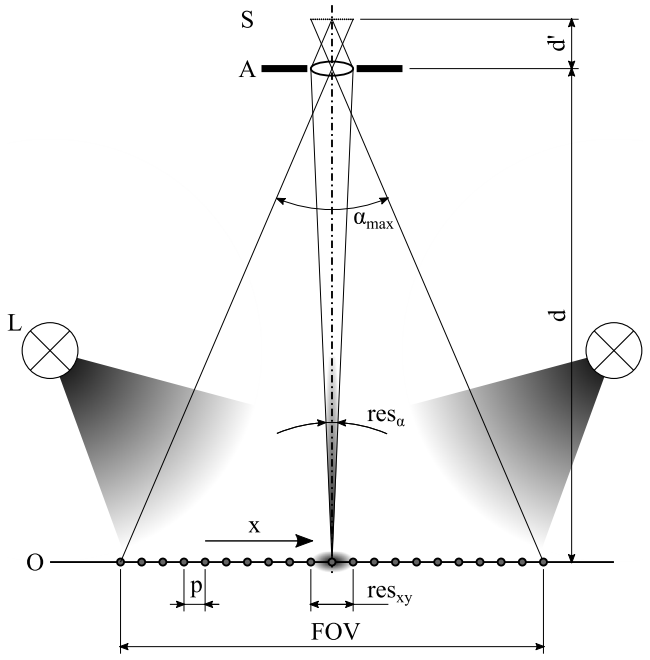

FIGURE 1. Configuration of the LF acquisition system: The system consists of a single sensor *S*, with an aperture *A*, and light sources *L* (two of the four light sources are depicted in the figure). The inspected object is located in a plane *O*. *d* and *d'* are the object and image distances with respect to the aperture. The aperture opening defines the size of the observed light res_α and the lateral resolution res_x. *p* is the lateral sampling. *x* is the direction of transport in the inline acquisition process. If an object point moves entirely across the FOV it can be observed in the angular range α_{max}.

  - Photoneo PhoXi XS, a structured light depth sensor
  - Keyence LJ-X8400, a laser line triangulation sensor
  - Chromasens 3DPIXA dual (30 μm) a stereo line-scan camera
- Demonstration of advantages and disadvantages of various acquisition types

II. INLINE LIGHT FIELD (LF) ACQUISITION SYSTEM

The inline LF acquisition system comprises a sensor head, optics, and a strobed illumination. For the inline acquisition process only a single camera and lens is used, still 3D information can be obtained by two complementary information sources: First the system relies on an endocentric projection, which means that every point in the field of view is captured with a different observation angle (see Fig. 1). As the object travels entirely across the FOV during the acquisition process, every point on the object is seen under the full angular range of the camera. From these multiple views MVS can be calculated. Second, the object is illuminated from four illumination directions (north / south normal to the transport direction and west / east along the transport direction). For each sensor exposure, only one illumination is active, which is then used to suppress matching ambiguities in the stereo matching process [36].

A. LIGHT FIELD ACQUISITION HARDWARE

A schematic overview of the acquisition system is depicted in Fig. 1. Previously, the object was acquired by sampling single lines, sparsely distributed along the transport direction (multi line–scan ICI) [29]. As the full scene has to be illuminated, it is more efficient to capture full area images (area–scan ICI) [36]. A frame is captured periodically during the object's continuous motion. The distance the object has moved between two consecutive acquisitions is denoted as s. Hence the acquisition system works similarly to a linear LF-camera array.

The number and density of such a LF camera array, the focal length, aperture setting, and sensor sampling determines the accuracy of the depth estimation and the Depth of Focus (DOF) [38]. Adapting these parameters to the proposed single-sensor ICI system, optical and accuracy parameters can be deduced: The focal length f defines the FOV for a given camera and working distance d. In addition, it is critical to correctly set the optics aperture "f-Number" ($f/\#$) as it defines the near and far focal distances (d_F and d_N) as described by (1) and (2), and thus the DOF (3) for a certain accepted circle of confusion c [38], [39]:

$$d_F = \frac{f^2 d}{f^2 + f/\# \cdot c(f-d)} \tag{1}$$

$$d_N = \frac{f^2 d}{f^2 + f/\# \cdot c(d-f)} \tag{2}$$

$$DOF = d_F - d_N \tag{3}$$

The focal length f, working distance d, and the sensor's pixel pitch p' define the lateral sampling p (4):

$$p = p' \cdot \frac{d}{d'} \tag{4}$$

As depicted in Fig. 1, every field point is observed from a different perspective defined by the entrance pupil as projection center. Thus the data points, captured during a single sensor exposure, are spread across the lateral FOV and the angular range of α_{max}. In the ray space representation (see Fig. 2), this resembles data points on a diagonal line. The aperture defines an observation cone angle res_α. The angle res_α can be interpreted as the angular ambiguity or uncertainty for the sampled object point. This results in $n = \alpha_{max}/res_\alpha$ independent angular observations. The LF can be considered to be sampled densely, if there are no gaps between the angular and spatial observations from individual sensor exposures, or, in other words, if the entire spatial and angular observation range is captured without gaps. To achieve the acquisition of all object points at all possible observation angles, an image has to be acquired after the object has traveled $s = FOV/n$, where s is equal to the entrance pupil diameter of the optics. Using this step size in between single acquisitions the sampling of the LF corresponds to the gray dots in Fig. 2. In analogy to the ambiguity of the angular sampling, the lateral resolution res_{xy} of the imaging system can be interpreted as the spatial uncertainty. Considering the angular and spatial uncertainty of the sampled points, the LF is densely sampled. Given the acquisition optics, it follows that every object point is observed from every possible direction. This results in maximal robustness, e.g. against reflections in

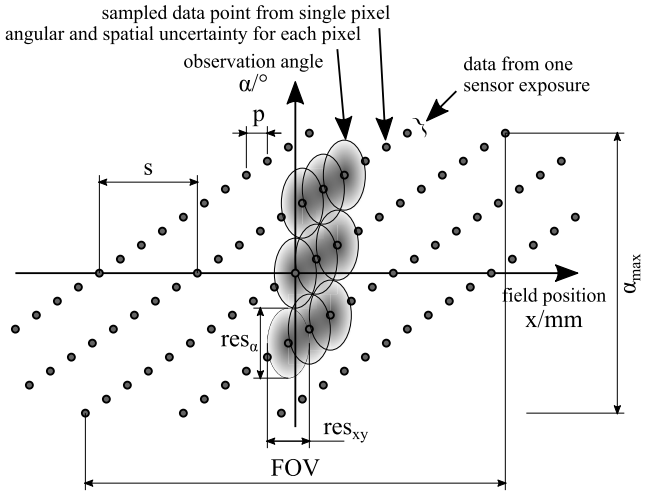

FIGURE 2. Ray space diagram for visualization of the LF sampling: The coordinate axes represent the observed object's field position *x* in transport direction and the viewing angle α. Each acquired image spans across the FOV in *x*-direction. Each sampled point (sensor pixel) corresponds to one gray dot. Considering the pinhole camera projection from (Fig. 1) the viewing angle spreads across α_{max}. During transport, images are acquired sequentially. Whereas the camera always sees the same angular range, the object moves by the distance *s* between images. The spatial optical resolution res_{xy} and the observation cone angle res_{α}, describe the measurement's uncertainty.

particular directions. This densely sampled LF is acquired for all four illumination directions. This additionally increases the robustness against specular reflections or shadows in the stereo matching process.

B. COMPUTATIONAL IMAGING ALGORITHMS

The input data for the computational imaging algorithm are four densely sampled LFs. Each LF represents the object from a different illumination direction (N / S / W / E). For every image, corresponding to an observation of the object at a specific location, features with the sizes of 11 × 11 and 15 × 15 pixels are calculated. Similar to classical MVS, disparity maps can be calculated by means of matching the calculated features with features of locations before and after the current location. In contrast to a simple stereo setup with two cameras, the depth from a single object point can be estimated by a large number of different multi-view matches, as the full LF rather than only two views are acquired. During the process of fusing the vast number of depth estimations for each object point, different consistency checks can be done: the disparities can be calculated and compared between forward and backward direction, consistency of depth estimates from different feature sizes can be compared and matching ambiguities can further be detected by comparing the four illumination directions. The latter especially helps for inconsistencies in the feature matching, arising from different appearances when illuminated from different directions e.g. specular reflections at specific constellations of viewing and illumination direction angles. Further details regarding the algorithms are explained in dedicated publications [35], [36].

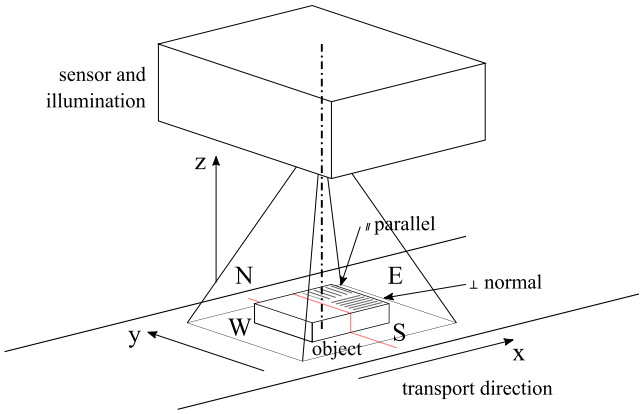

FIGURE 3. Definition of the orientations (N, S, W, E) and coordinate system for comparing the different acquisition devices. Principal orientations of small surface structures are denoted ⊥ if they are oriented along the *x* coordinate and ∥ if they are oriented parallel to the *y* coordinate.

III. EXPERIMENTS AND EVALUATION

A quantitative and qualitative comparison of the different inline optical 3D measurement systems is performed by conducting the following experiments:

- Flat slope: A textured flat surface slope is acquired. The slope is designed to fill the whole FOV and DOF. It is placed in four different orientations (''North'', ''South'', ''West'', ''East'', see Fig. 3 for the orientation definition). Two consecutive measurements are performed for each orientation, see Fig. 4 a).
- USAF Target: lateral resolution (texture resolving power) is measured by using a USAF target at three heights across the depth range.
- Surface roughness normal: A standardized surface roughness reference normal with known surface statistics is used to statistically characterize spatial smoothing filters and the reconstruction quality of fine surface structures, see Fig. 4 b).
- Real world example: this scene comprises different challenging objects, arranged within the acquisition volume, see Fig. 4 c).

The following sub-sections describe how comparable measurements are deduced from the experiments.

A. MEASUREMENT NOISE AND HEIGHT RESOLUTION

The temporal measurement noise can be determined by the subtraction method [6], [41]:

> ''The pointwise difference is calculated between two immediately consecutive measurements of a planar surface in the same position, under ideal laboratory and measurement conditions. The S_q parameter is calculated from the S-F surface without using an S filter, see (5). The result is divided by $\sqrt{2}$. There may be no time-related averaging and no optional filtering of measurements; only signal processing specific to the procedure is permitted.''

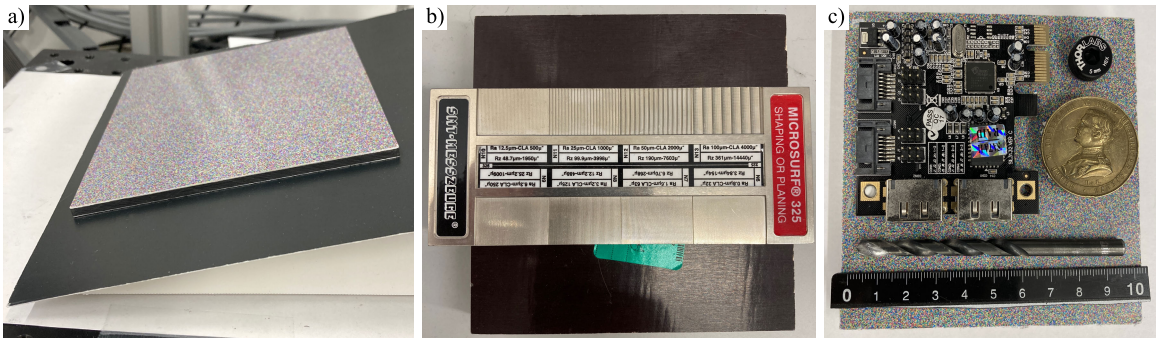

FIGURE 4. Objects used for the experiments: a) textured flat surface, b) standardized roughness target, c) mixed real world scene.

The S_q parameter is defined in [37]:

$$S_q = \sqrt{\frac{1}{A}\iint_A z^2(x,y)dxdy} \tag{5}$$

$z(x, y)$ is the pointwise difference between two consecutive measurements at the object location (x, y); a Root Mean Square (RMS) is calculated for the entire measurement area A. To stabilize the estimate, the measurement is repeated several times as proposed by the Fair Data Sheet [6]. For this comparison, eight measurements are performed on a planar textured slope. The eight measurements are two consecutive measurements for each slope orientation (''North'', ''East'', ''South'', ''West''). A is chosen to cover an area of 100 mm × 100 mm. The estimated measurement noise $\overline{N_M}$ is evaluated as follows:

$$\overline{N_M} = \frac{1}{n \cdot \sqrt{2}} \sum_{i=1}^{n} S_{q,i} \tag{6}$$

Here $S_{q,1} - S_{q,4}$ are the four S_q-values as defined by (5), for the four acquired orientations of the flat surface. Because of preferential measurement directions, e.g. caused by sensor or light orientations, the S_q value is different for each of the four orientations; the individual S_q-values are given in Table 2.

Assuming a normal distribution of measurement noise, the smallest distinguishable height measurement being detected with a 95% confidence interval, res_z can be calculated from the measurement noise [6]:

$$res_z = \overline{N_M} \cdot \sqrt{8} \tag{7}$$

The height resolution, hence the distribution of the measurements for the same true value, is also sometimes denoted as the measurement precision as depicted in Fig. 5.

B. LATERAL RESOLUTION

Although often used incorrectly in data-sheets, the lateral resolution must not be confused with the measuring point spacing (=sampling). To prevent confusion in this paper we always use the unit μm/pixel to describe the lateral sampling. Optical resolution is defined as the distance between two barely distinguishable features of an object. For features of the object's texture, the minimal theoretically resolvable distance $res_{xy_{dl}}$ is limited by optical diffraction and can be

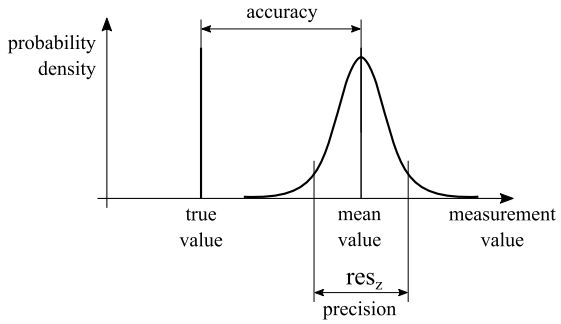

FIGURE 5. The accuracy is the distance between the reference value and the measured mean value. Precision describes the distribution of the measured values, adapted from [38] .

calculated with the Rayleigh criterion from the objective's numerical aperture NA [6]:

$$res_{xy_{dl}} = \frac{0.61 \cdot \lambda}{NA} \tag{8}$$

where λ is the central wavelength. The NA is typically defined for microscope optics, whereas macroscopic lenses are characterized by their ''f-number'' $f/\#$, which can be used to estimate the maximum theoretical optical resolution using Rayleigh's criterion:

$$res_{xy_{dl}} = 2.44 \cdot \lambda \cdot f/\# \cdot \frac{d}{d'} \tag{9}$$

Defocus, optical aberration, motion blur in the transport process, sampling and post-processing further deteriorate the optical resolution. Thus, the true lateral resolution res_{xy} has to be measured experimentally. A USAF resolution test chart EdmundOptics #38-710 was acquired [42]. Table 2 res_{xy} denotes the inverse of the smallest resolvable group-element in the specified experiment. Note that this analysis is purely based on the resolution on texture features (brightness values). As lateral 3D features (height values) are generated on a fundamentally different basis, the res_{xy} is not directly connected to the resolution with which 3D features can be reconstructed.

C. CALIBRATION ACCURACY

Precision is defined as the distribution of the measured values around the mean value, which is described via the resolution

TABLE 1. Tested devices and data sheet specifications. [1)] not specified – derived from FOV and 3200 pixel sensor width, [2)] asymmetric +95/−220 mm, [3)] the system is designed to capture a static scene and not for moving objects, [4)] 380 · tan(17.65°), [5)] Z-Linearity = 0.0025% of 120 mm for an operation range of ±60 mm around the reference distance, [6)] no specification given in the data sheet; data sheet value "z-axis repeatability" (=5 μm) differs from the definition in Equation 6 as the height measurement is averaged along a 30 mm line, [7)] the data sheet shows a "height resolution" of 5 μm, according to correspondence with the manufacturer this represents the "height-difference per pixel disparity and the precision of the correlation algorithm" thus id does not follow the definition given in in Equation 6, [8)] estimated from technical drawing, [9)] no specification given in the data sheet, [10)] ICI and 3DPIXA require an illumination which is positioned closer to the object than the objective's Working Distance (WD).

	AIT ICI 50μm	Photoneo PhoXi XS	Keyence LJ-X8400	Chromasens 3DPIXA dual 30μm
Principle	single sensor LF MVS & PS	structured light multi frame	laser line triangulation	stereo camera
Sampling p / μm/pixel	50	55	65 [1)]	30
FOV / mm	116	78 × 113	210	210
WD d [10)] / mm	195	181	380	282.3
Baseline mm	multiple up to 86.3	85	121 [4)]	100 [8)]
Calibration Accuracy a / μm	50	35	30 [5)]	– [9)]
Temporal noise $\overline{N_M}$ / μm	5	30	– [6)]	– [7)]
Acquisition Speed	for 33 independent views 48M Points / s	full scan 0.25 - 2 s [3)] 16M Points / s	16 kHz line rate 52M Points / s	29,7 kHz line rate 208M Points / s
Acquisition Speed / mm/s	1000	(428) [3)]	1040	891
DOF / mm	38	44	315 [2)]	11.2

in depth res_z. Accuracy is defined by the difference between the true reference value and the mean measured values a, see also Fig. 5. A detailed theoretical analysis for precision and accuracy in optical depth estimation was done by Diebold et. al. [38]. An accurate system calibration is crucial for its measurement accuracy. For an experimental analysis, accurate reference values are needed.[1] For characterizing the systems accuracy an experimental assessment of the system's calibration regarding depth measurements is performed: The flatness of the reference slope was confirmed by a tactile coordinate-measuring machine to be < 10μm in the investigated 100 mm × 100 mm area. This value is smaller than the obtained depth resolution res_z for all tested systems. The texture is a random color-pattern with a spatial frequency of 5 dots per millimeter. The spatial frequency was chosen to be lower than the system's optical resolution to ensure that the texture has detectable features despite of image aberrations and defocus. The texture was produced with a professional color printer on a semi-matt surface, the object is depicted in Fig. 4 a). The reference slope was imaged in four orientations of the slope direction (N / S / W / E). For an experimental evaluation of the calibration accuracy, a plane is fitted in a way that the measurement points have least square distance to the fitted plane. The deviation δ between the measured height and the fitted reference plane reveals how height measurements systematically deviate across the FOV and DOF. With that we determine the calibration accuracy a as:

$$a = 2 \cdot \sigma(\delta) \tag{10}$$

With the factor two, 95% of the measurements deviate less than $\pm a$ with respect to the reference.

[1]It is impossible to get accurate absolute height values with respect to the sensor. Regarding practical applications, only relative measurements with respect to other objects features are of interest. Thus the accuracy analysis is only performed in the domain of relative measurements within the acquisition volume

D. SMOOTHING CHARACTERISTICS

For simple surface structures the depth resolution, as given by (7), can be improved arithmetically by applying spatial smoothing or by using large feature sizes for the 3D depth estimation. Contrary to an improved depth resolution, smoothing filters would compromise the detection of fine surface structures. To quantify smoothing characteristics, a standardized surface roughness normal is acquired.

The roughness normal is a "Microsurf 325 for shaping/planing" with a unidirectional roughness pattern. Four Region of Interest (ROI)s were used:

- N13: Ra = 100 μm, Rz = 361 μm, l_P = 3.2 mm
- N12: Ra = 50 μm, Rz = 190 μm, l_P = 1.6 mm
- N11: Ra = 25 μm, Rz = 99.9 μm, l_P = 1.1 mm
- N10: Ra = 12.5 μm, Rz = 48.7 μm, l_P = 450 μm

Ra is the center line average roughness and Rz the average maximum height of the profile (average across 5 independent sections) according to EN ISO 4287; l_P is the lateral periodicity of the roughness pattern.

The surface roughness normal was acquired twice, once with the surface ripples along the x-direction ($\perp$) and once with the ripples along the y-direction ($\parallel$) - see Fig. 3.

E. REAL WORLD EXAMPLE

For the qualitative assessment we used an artificial scene comprising a PCB, a machine drill, a coin, a ruler and a hand screw. The choice of objects highlight the different challenges like gloss, dark areas and complex surface geometries including occlusions. All devices use internal confidence filters to eliminate occluded areas or flawed measurements. To compare the robustness of the different devices, the fraction of measurement points covered with confidence is evaluated.

IV. EXPERIMENTAL RESULTS

In this section, the technical parameters, given in the manufacturers data-sheets are summarized and compared with the

TABLE 2. Performance parameters from experimental measurements. Notes: [1] Resolution in μm is experimentally derived from the inverse of the grid pattern in lp/mm which could be resolved with a contrast of > 25%, mean value between x and y; [2] derived from Equ. 7.

	AIT ICI 50μm	Photoneo PhoXi XS	Keyence LJ-X8400	Chromasens 3DPIXA dual 30μm
S_q / μm in N / S / W / E orientation	5.9 / 5.6 / 6.8 / 6.2	7.4 / 8.0 / 11.8 / 6.6	20.1 / 9.4 / 16.5 / 13.6	5.7 / 7.3 / 11.8 / 14.7
Height Resolution res_z / μm	12.2	17.0	29.8	19.7
Calibration accuracy a / μm	41.3	59.8	97.2	41.4
Lateral Resolution res_{xy} / μm[1)] WD+15mm / WD / WD-15mm	200 / 140 / 200	140 / 140 / 140	250 / 250 / 250	250 / 100 /281
Estimation for Ra=100 μm (Rz=361 μm) $\perp$ / $\parallel$	83.7 / 152.2 (281 / 424)	99.8 / 99.2 (386 / 381)	100.0 / 085.4 (427 / 412)	101.0 / 65.5 (399 / 243)
Estimation for Ra=50 μm (Rz190 μm) $\perp$ / $\parallel$	45.7 / 078.4 (121 / 234)	52.3 / 52.2 (238 / 229)	075.9 / 124.3 (309 / 587)	036.5 / 56.3 (163 / 249)
Estimation for Ra=25 μm (Rz=99.9 μm) $\perp$ / $\parallel$	22.6 / 100.2 (111 / 395)	21.4 / 18.1 (122 / 102)	050.2 / 066.4 (250 / 316)	014.4 / 13.3 (081 / 068)
Estimation for Ra=12.5 μm (Rz=48.7 μm) $\perp$ / $\parallel$	19.7 / 074.8 (068 / 268)	11.6 / 47.6 (068 / 246)	033.5 / 133.7 (177 / 463)	004.2 / 08.7 (031 / 034)

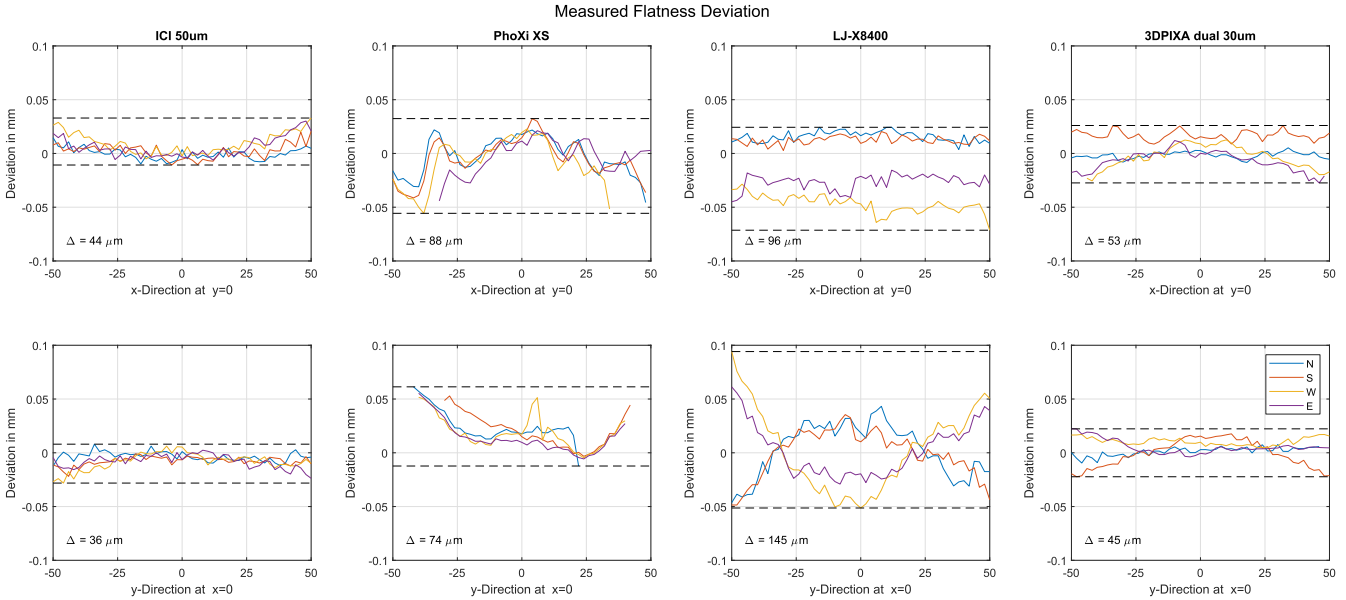

FIGURE 6. The plots depict the deviation between the depth measurement of a flat reference surface and the true flat plane. For a compact visualization only the deviation along $y = 0$ mm (upper row) and $x = 0$ mm (lower row) are depicted. For each system the test is performed for four different orientations (N / S / W / E) of the reference plane.

quantitative evaluation results. For a qualitative comparison the reconstructions of the real world example are presented side-by-side.

A. TEST DEVICES

Most manufacturers deliver their system in different ranges, we chose a range with the best overlap between different measurement principles. For a meaningful comparison we chose systems with a point-to-point sampling closest to 50 μm. Considering the sampling limit according to the Nyquist criterion a lateral optical resolution of 100 μm is possible. For a conventional setup, with the sensor parallel to the object and transport plane, the 100 μm optical resolution limit allows for a DOF of 30 to 40 mm (see (3) and (9)). Some of the technologies allow for high acquisition speeds when reconstruction speed is compromised. For a fair comparison all systems are tested at their settings for best reconstruction quality. The selected devices which were compared in this analysis are listed in Table 1. The table includes the data-sheet specification.

B. MEASUREMENT RESULTS - QUANTITATIVE ANALYSIS

Table 2 depicts the analysis results for the **depth resolution** res_z deduced from the temporal noise as described in (7). Some systems have a preferential direction due to their measurement principle. Thus, the individual S_q value is given for every orientation of the reference plane.

Considering the sampling theorem the diffraction limited optical resolution $res_{xy_{dl}}$ should not be smaller than two times the lateral sampling to avoid aliasing; the sampling itself limits the **lateral resolution** res_{xy} to 100 μm for AIT ICI, 110 μm for Photoneon PhoXi, 130 μm for Keyence LJ-X8400 and 60 μm for Chromasens 3DPIXA. True values, obtained experimentally, are given in Table 2 for three different working distances (reference distance and $\pm$ 15 mm). Note that the $\pm$ 15 mm are outside the specified depth range of the Chromasens 3DPIXA.

The measurement and **calibration accuracy** a is depicted in Fig. 6. From every slope orientation (N/S/W/E), we obtain a 2D map which describes the deviation between the

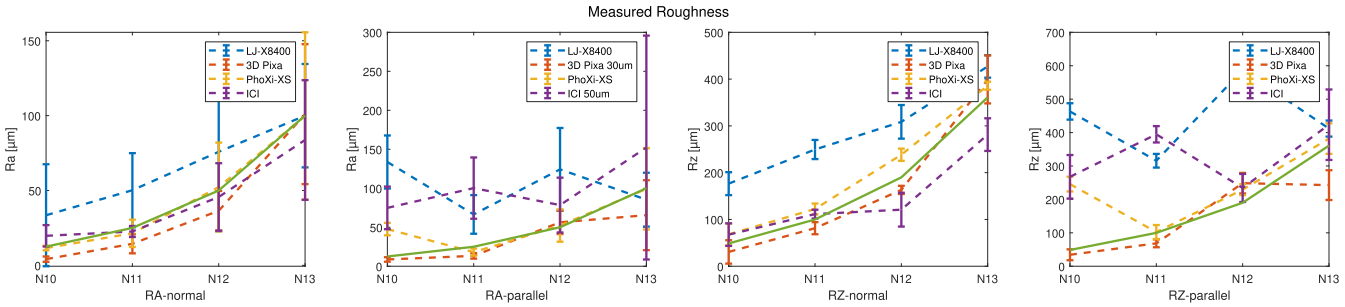

FIGURE 7. Comparison of true and measured surface statistics parameters. Surface statistics are compared by average roughness Ra and the profile height Rz both in parallel and normal orientation (see Fig. 3). The green line depicts the true value given by the surface normal, dashed lines are the measurement results. Ra and Rz can be calculated along approximately 150 lines within the size of the roughness target, error bars are $\pm\sigma$ fo all Ra/Rz measurements.

TABLE 3. Qualitative comparison of the 3D reconstruction results on a challenging real world scene. The scene comprises a PCB with pin headers, a coin, black anodized aluminum screw, a drill and a black plastic ruler. Colormaps are equally scaled for all four systems, dark blue areas represent areas where the measurement devices do not deliver confident measurement points. Notes: [1)] percentage of the total FOV which is covered by confident measurement points.

	AIT ICI 50um	Photoneo PhoXi XS	Keyence LJ-X8400	Chromasens 3DPIXA dual 30um
confident[1)]	95.9%	83.5%	98.9%	84.5%
Full	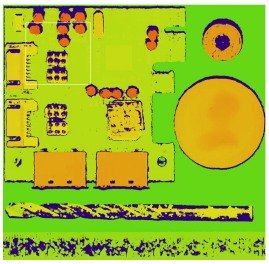	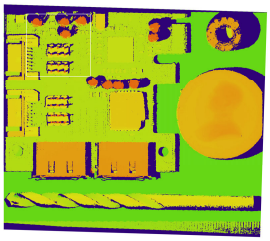	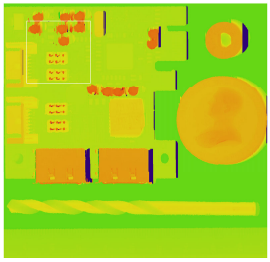	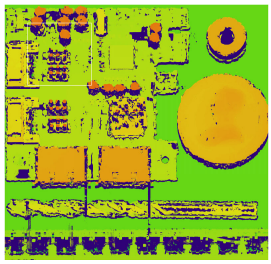
Crop	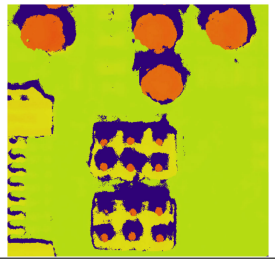	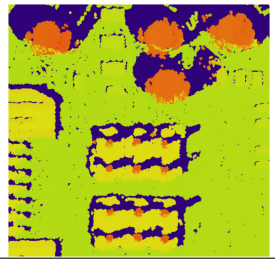	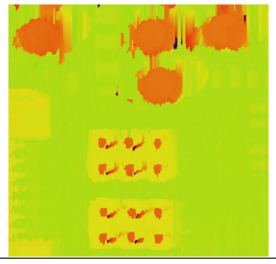	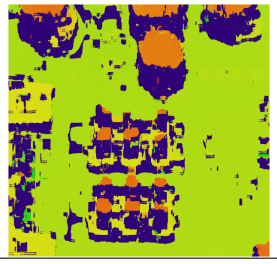

Colormap: non confident areas 0 mm 20 mm

measurement points and the flat sloped reference surface. To reduce the data for visualization two cross-section (at $x = 0$ mm and $y = 0$ mm) are depicted for each slope orientation.

Fig. 7 and Table 2 show the **surface structures**. As the roughness reference object is a glossy object, it is challenging for optical inspection. The results are expected to be noisier than it might be assumed from the measured temporal noise. If surface regularization is applied in the 3D reconstruction pipeline, surface N10 with a lateral periodicity of only $l_P = 450$ μm should be affected the most by the surface smoothing. Still, as the 450 μm are well above the resolution limit, the systems should be able to resolve the surface roughness.

C. QUALITATIVE COMPARISON

For a general qualitative comparison the real world example, as described above, is acquired with all four devices. As only an overview image and a crop of one area can be shown in this paper, these four acquisitions are provided as *.ply - file in the supplementary materials [43] to be viewed and compared in open source software like cloud-compare [44]. No preprocessing other than conversion to a common file format was done. The height maps are depicted in Table 3.

V. DISCUSSION

For an objective and conclusive comparison, all experiments were performed with the same parameters for all experiments and no parameter optimization was done for the individual

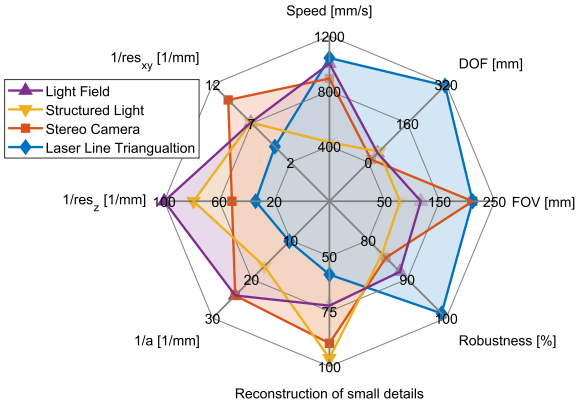

FIGURE 8. Spider web diagram for comparing the four different acquisition systems. Speed is the maximal acquisition speed, DOF is the maximal depth range, and FOV along the *x*–direction according to the data sheet. Robustness corresponds to the percentage of confidently covered points in the real world scene (see Table 3, the reconstruction of small details is deduced from the average performance of accurately measuring the Ra-values for the N11 and N12 surface roughness, $\frac{1}{a}$ describes the measured calibration accuracy (see (10)), $\frac{1}{res_z}$ describes the measured depth resolution (see (7)) and $\frac{1}{res_{xy}}$ the measured optical resolution at the nominal working distance. – Partly inverse values are given so that in any case a larger value corresponds to a better system performance.

experiments. We want to point out, as AIT ICI is our own development, we have better control in the general handling than for the other systems. All manufactures had been contacted with an intermediate report of the test results to mitigate potential user errors. Fig. 8 summarises the observed performance parameters for all systems. We compare acquisition speeds in mm/s rather than acquired point number in M Points/s, as this is the relevant parameter for the industrial application use-case as mentioned in the introduction. Some observations can be explained by general physical limitations, others are specific to the measurement principle. These observations will be discussed in this section.

A. GENERAL THEORETICAL LIMITATIONS

1) LATERAL RESOLUTION VS. DOF

In Fig. 8, an opposing order in the depth range (DOF) and the lateral resolution ($\frac{1}{res_{xy}}$) can be observed. Due to diffraction a good lateral optical resolution res_{xy} requires a small "f-number" $f/\#$ (see (9)), but in return deteriorates the DOF (see (1) - (3)). It is impossible to overcome this limitation for measurement principles where the sensor is oriented parallel to the object plan. This observation is also in line with the datasheet specifications (see Table 1) - the stereo camera system with the smallest sampling of 30 μm/pixel, and thus the best possible optical resolution, has the smallest DOF.

2) ROBUSTNESS VS. ACCURATE RECONSTRUCTION OF SMALL SURFACE DETAILS

With standard settings for filtering non confident points, the point cloud from laser line triangulation system covers almost 100% of the object's surface. It seems that in general this comes at the cost of the reconstruction of small surface details. Fig. 8 reveals an opposing order of the system's robustness and accuracy in the surface roughness measurements. Thus we assume that a good control in outlier detection and smoothing in the post processing is more important for the reconstruction of small surface details than the measurement principle itself.

3) CALIBRATION ACCURACY

In Fig. 8 it can be seen that systems with a good lateral resolution (high value for $\frac{1}{res_{xy}}$) show a good calibration accuracy (high value for $\frac{1}{a}$). This observation is very conclusive as during the calibration process, systems with a better optical resolution are capable of a superior determination of the camera calibration such as intrinsic-, extrinsic-, and distortion-parameters.

B. OBSERVATIONS SPECIFIC TO THE MEASUREMENT PRINCIPLES

1) 3D FROM LIGHT FIELD (LF)

Our AIT ICI - system shares strengths and weaknesses of 3D imaging systems. Equal to the stereo camera system it only relies on surface texture features, which are problematic on dark and smooth surfaces (e.g. the drill and the black plastic ruler on artificial test scene Fig. 4 c) and Table 3).

Texture based systems benefit from a simpler calibration procedure: In contrast to systems with an active illumination (in this case both the projected light pattern or laser line, as well as the imaging optics itself can be distorted), with the passive illumination only the imaging optics have to be corrected. This might be an additional reason for the observed superior calibration accuracy.

AIT ICI shows a very good temporal noise behavior and thus a good depth resolution. By incorporating the information form the full acquisition of the LF it has the maximal amount of information for depth estimation. As the LF can only be captured along the transport direction the system shows a preference in the orientation of surface features. As shown in Fig. 7 the system is excellent in measuring the surface roughness for structures oriented along the transport direction and considerably poor for structures along the y-axis.

2) STRUCTURES LIGHT PATTERN PROJECTION

The tested pattern projection system is the Photoneo PhoXi XS. In contrast to the other systems, this device is not meant for inline inspection of moving objects.

With standard settings for the confidence filter, it does a good job in removing non confident points resulting in a superior measurement of the surface roughness on a challenging glossy object. This comes at the cost of a quite low coverage of the object's surface with data-points (missing data points on the black thumb-screw and ruler - see Fig. 4 c) and Table 3). Additionally, there is a principal limitation of

areas which cannot be reached by the pattern projector due to occlusions (large ''shadow'' on the east-side from protruding objects).

We note that the measured height resolution is significantly lower than the specified value in the product data sheet which can be deduced from the specified temporal noise N_M and (7). We note that each product developer uses their own internal specification method. Therefore using a generalized method as e.g. proposed in the ''Initiative Fair Data Sheet'' [6], the manufacturer could have given a better value for the temporal noise as specified in the data sheet.

In Fig. 6 we observed systematic deviations in the calibration which exceed the manufactures specifications. This problem had been discussed with the manufacturer: It has to be pointed out that the calibration was done at the site of the manufacturer's for a valid range of between 22 °C - 25 °C and for white objects with 80 % albedo. Afterward the device was sent over to our lab where no further calibration was done. The manufacturer wants to emphasise that recent models are delivered with an enhanced calibration model and a possibility for rechecking the calibration after installation.

3) LASER LINE TRIANGULATION

The tested laser line triangulation system is the Keyence LJ-X8400.

Making use of the Scheimpflug-principle [45], it is possible for the line triangulation sensor to position the focus plane congruent to the laser illuminated plane, thus this sensor principle allows for the largest depth range and acquisition volume which differs significantly compared to other systems. It has to be mentioned the full specified depth range requires a larger read-out area on the sensor and thus would deteriorate the specified acquisition speed.

The deviations at the roughness target and the comparability with the sensor parameters were discussed with the manufacturer: The large temporal noise might be an explanation for the over-estimation of the surface roughness. This especially occurs if surface structures are oriented parallel to the projected laser line and close to the resolution limit. Additionally, the sharp spikes of the roughness target can have a strong impact on the reflection angle and therefore produce errors.

4) STEREO CAMERA SYSTEM

As an example for an inline 3D stereo camera system, we tested the Chromasens 3DPIXA 30um. The system has a significantly higher lateral resolution compared to the other systems. Resulting effects have to be kept in mind when comparing systems with different resolutions.

As the system is a texture based stereo system, its calibration accuracy, as in the AIT ICI system, does not depend on the calibration of an active illumination.

In Table 3, the crop-detail reveals that in the depth image regions with higher z-values are shifted towards the y-direction. We are not aware of the particular reason, but the shift could be undone by a simple geometric transformation. This was not done to preserve the integrity of the data as they come from the manufacturer's software. Additionally the crop reveals severe block artefacts. According to the manufacturer this can be due to a sub-optimal selection of the selected window size for 3D-feature correlation. Nevertheless, the system still shows very good results for the roughness estimation. Regarding the z-resolution, the manufacturer states, that they estimate their z-resolution with the theoretical value based on their matching algorithm, without the 95% confidence interval. For a real world sample, their height measurement would consist of hundreds of points which are used for a single height estimation.

C. CONCLUSION

Fig. 8 highlights that the systems cover complementary areas in the eight dimensions investigated in this paper. As pointed out above, some predominant benchmarks are mutually exclusive due to principal limitations.

In the authors' opinion it is very hard to deduce the benefits from the provided data-sheets. For even very fundamental parameters like the lateral optical resolution is specified in none of the data-sheets according to the definitions given by standards or the ''Initiative Fair Data Sheet'' [6]. Or, as another example, the term ''depth resolution'' is either used incorrectly or does not conform to established definitions, comprehensible for the end user.

This research will support the community in the field of optical 3D inspection on two ends: On the one hand, users can use the provided methods and results to gain a better understanding of the benefits which come with different measurement principles. On the other hand, we encourage manufacturers to specify their products according to applicable standards. To our knowledge, this is the first experimental comparison of different 3D reconstruction methods in this comprehensible manner, using established standards.

ACRONYMS

DOF	Depth of Focus
FOV	Field of View
ICI	Inline Computational Imaging
LF	Light Field
MVS	Multi View Stereo
PS	Photometric Stereo
WD	Working Distance
ROI	Region of Interest
RMS	Root Mean Square

ACKNOWLEDGMENT

The authors thank the manufacturers who provided samples of their devices enabling the comparison of different measurement principles.

REFERENCES

[1] H. Golnabi and A. Asadpour, "Design and application of industrial machine vision systems," *Robot. Comput.-Integr. Manuf.*, vol. 23, no. 6, pp. 630–637, Dec. 2007. [Online]. Available: http://www.sciencedirect.com/science/article/pii/S0736584507000233

[2] E. Savio, L. De Chiffre, and R. Schmitt, "Metrology of freeform shaped parts," *CIRP Ann.*, vol. 56, no. 2, pp. 810–835, 2007.

[3] Y. Deng, X. Pan, X. Wang, and X. Zhong, "Vison-based 3D shape measurement system for transparent microdefect characterization," *IEEE Access*, vol. 7, pp. 105721–105733, 2019.

[4] F. Blais, "Review of 20 years of range sensor development," *J. Electron. Imag.*, vol. 13, no. 1, pp. 231–243, 2004, doi: 10.1117/1.1631921.

[5] G. Sansoni, M. Trebeschi, and F. Docchio, "State-of-the-art and applications of 3D imaging sensors in industry, cultural heritage, medicine, and criminal investigation," *Sensors*, vol. 9, no. 1, pp. 568–601, Jan. 2009.

[6] *Definition of a Comparable Data Sheet for Optical Surface Measurement Devices. Version 1.2*, Fair Data Sheet Initiative, Physikalisch-Technische Bundesanstalt, Braunschweig, Germany, 2016.

[7] H. Schwenke, U. Neuschaefer-Rube, T. Pfeifer, and H. Kunzmann, "Optical methods for dimensional metrology in production engineering," *CIRP Ann.*, vol. 51, no. 2, pp. 685–699, 2002.

[8] F. Chen, G. M. Brown, and M. Song, "Overview of 3-D shape measurement using optical methods," *Opt. Eng.*, vol. 39, no. 1, pp. 10–22, 2000, doi: 10.1117/1.602438.

[9] E. Lilienblum and A. Al-Hamadi, "A structured light approach for 3-D surface reconstruction with a stereo line-scan system," *IEEE Trans. Instrum. Meas.*, vol. 64, no. 5, pp. 1258–1266, May 2015.

[10] J. Geng, "Structured-light 3D surface imaging: A tutorial," *Adv. Opt. Photon.*, vol. 3, no. 3, pp. 128–160, Mar. 2011. [Online]. Available: http://aop.osa.org/abstract.cfm?URI=aop-3-2-128

[11] S. Zhang, "Recent progresses on real-time 3D shape measurement using digital fringe projection techniques," *Opt. Lasers Eng.*, vol. 48, no. 2, pp. 149–158, Feb. 2010. [Online]. Available: http://www.sciencedirect.com/science/article/pii/S0143816609000529

[12] L. Lu, Y. Ding, Y. Luan, Y. Yin, Q. Liu, and J. Xi, "Automated approach for the surface profile measurement of moving objects based on PSP," *Opt. Exp.*, vol. 25, no. 25, pp. 32120–32131, Dec. 2017. [Online]. Available: http://www.opticsexpress.org/abstract.cfm?URI=oe-25-25-32120

[13] C.-H. Cho, Y.-S. Ku, P.-Y. Chang, H.-W. Lee, C.-W. Lo, and Y.-C. Chen, "System for measuring three-dimensional micro-structure based on phase shifting fringe projection," in *Proc. Int. Wafer Level Packag. Conf. (IWLPC)*, Oct. 2019, pp. 1–6.

[14] S. J. N. Drvar, "The assessment of structured light and laser scanning methods in 3D shape measurements," in *Proc. 4th Int. Congr. Croatian Soc. Mech.*, 2003, pp. 237–244.

[15] M. M. Auerswald, A. von Freyberg, and A. Fischer, "Laser line triangulation for fast 3D measurements on large gears," *Int. J. Adv. Manuf. Technol.*, vol. 100, nos. 9–12, pp. 2423–2433, Feb. 2019.

[16] A. Miks, J. Novak, and P. Novak, "Analysis of imaging for laser triangulation sensors under scheimpflug rule," *Opt. Exp.*, vol. 21, no. 15, pp. 18225–18235, Jul. 2013. [Online]. Available: http://www.opticsexpress.org/abstract.cfm?URI=oe-21-15-18225

[17] M. Alonso, A. Izaguirre, I. Andonegui, and M. Graña, "Optical dual laser based sensor denoising for OnlineMetal sheet flatness measurement using Hermite interpolation," *Sensors*, vol. 20, no. 18, p. 5441, Sep. 2020. [Online]. Available: https://www.mdpi.com/1424-8220/20/18/5441

[18] R. G. Dorsch, G. Häusler, and J. M. Herrmann, "Laser triangulation: Fundamental uncertainty in distance measurement," *Appl. Opt.*, vol. 33, no. 7, pp. 1306–1314, 1994.

[19] R. Tsai, "A versatile camera calibration technique for high-accuracy 3D machine vision metrology using off-the-shelf TV cameras and lenses," *IEEE J. Robot. Autom.*, vol. RA-3, no. 4, pp. 323–344, Aug. 1987.

[20] Z. Zhang, "Flexible camera calibration by viewing a plane from unknown orientations," in *Proc. 7th IEEE Int. Conf. Comput. Vis.*, vol. 1, Sep. 1999, pp. 666–673.

[21] J. Huang, Z. Wang, Q. Xue, and J. Gao, "Calibration of a camera–projector measurement system and error impact analysis," *Meas. Sci. Technol.*, vol. 23, no. 12, Oct. 2012, Art. no. 125402, doi: 10.1088/0957-0233/23/12/125402.

[22] V. Suresh, J. Holton, and B. Li, "Structured light system calibration with unidirectional fringe patterns," *Opt. Lasers Eng.*, vol. 106, pp. 86–93, Jul. 2018. [Online]. Available: http://www.sciencedirect.com/science/article/pii/S0143816617313210

[23] X. Xu, Z. Fei, J. Yang, Z. Tan, and M. Luo, "Line structured light calibration method and centerline extraction: A review," *Results Phys.*, vol. 19, Dec. 2020, Art. no. 103637. [Online]. Available: http://www.sciencedirect.com/science/article/pii/S2211379720320672

[24] A. Kadambi, A. Bhandari, and R. Raskar, *3D Depth Cameras in Vision: Benefits and Limitations of the Hardware*, L. Shao, J. Han, P. Kohli, and Z. Zhang, Eds. Cham, Switzerland: Springer, 2014.

[25] M. Hashimoto and K. Sumi, "3-D object recognition based on integration of range image and gray-scale image," in *Proc. Brit. Mach. Vis. Conf. (BMVC)*, T. F. Cootes and C. J. Taylor, Eds., Manchester, U.K., 2001, pp. 1–10.

[26] B. Sun, J. Zhu, L. Yang, S. Yang, and Y. Guo, "Sensor for in-motion continuous 3D shape measurement based on dual line-scan cameras," *Sensors*, vol. 16, no. 11, p. 1949, Nov. 2016.

[27] T. Ilchev, E. Lilienblum, B. Joedicke, B. Michaelis, and M. Schnitzlein, "A stereo line sensor system to high speed capturing of surfaces in color and 3D shape," in *Proc. GRAPP/IVAPP*, 2012, pp. 809–812.

[28] R. Calow, T. Ilchev, E. Lilienblum, M. Schnitzlein, and B. Michaelis, "Schnelles zeilensensorsystem zur gleichzeitigen erfassung von farbe und 3D-form," in *Forum Bildverarbeitung*. Karlsruhe, Germany: KIT Scientific Publishing, 2010, pp. 181–192.

[29] S. Štolc, D. Soukup, B. Holländer, and R. Huber-Mörk, "Depth and all-in-focus imaging by a multi-line-scan light-field camera," *J. Electron. Imag.*, vol. 23, no. 5, Oct. 2014, Art. no. 053020.

[30] D. Antensteiner, S. Štolc, K. Valentín, B. Blaschitz, R. Huber-Mörk, and T. Pock, "High-precision 3D sensing with hybrid light field & photometric stereo approach in multi-line scan framework," *Electron. Imag.*, vol. 2017, no. 9, pp. 52–60, Jan. 2017.

[31] D. Antensteiner, S. Štolc, and T. Pock, "A review of depth and normal fusion algorithms," *Sensors*, vol. 18, no. 2, p. 431, Feb. 2018.

[32] B. Blaschitz, S. Štolc, and D. Antensteiner, "Geometric calibration and image rectification of a multi-line scan camera for accurate 3D reconstruction," *Electron. Imag.*, vol. 2018, no. 9, pp. 1–240, 2018.

[33] N. Brosch, S. Štolc, and D. Antensteiner, "Warping-based motion artefact compensation for multi-line scan light field imaging," *Electron. Imag.*, vol. 2018, no. 15, pp. 1–273, 2018.

[34] L. Traxler and S. Štolc, "3D microscopic imaging using structure-from-motion," *Electron. Imag.*, vol. 2019, no. 16, pp. 1–3, 2019.

[35] S. Breuss, S. Štolc, L. Traxler, and B. Blaschitz, "Computer-implementiertes verfahren zur erstellung von mehrdimensionalen gegenstands-datenstrukturen," Austria Patent, Oct. 16, 2020.

[36] B. Blaschitz, S. Breuss, L. Traxler, L. Ginner, and S. Štolc, "High-speed inline computational imaging for area scan cameras," in *Society for Imaging Science and Technology*, 2021.

[37] *Geometrical Product Specifications (GPS)—Surface Texture: Areal—Part 2: Terms, Definitions and Surface Texture Parameters*, Standard ISO 25178-2:2012, 2012.

[38] M. Diebold, O. Blum, M. Gutsche, S. Wanner, C. Garbe, H. Baker, and B. Jähne, "Light-field camera design for high-accuracy depth estimation," *Proc. SPIE*, vol. 9528, Jun. 2015, Art. no. 952803.

[39] S. Mottelet, L. de Saint Germain, and O. Mondin, "Smart depth of field optimization applied to a robotised view camera," *J. Math. Imag. Vis.*, vol. 44, no. 1, pp. 1–18, Sep. 2012.

[40] G. M. Pettersson, M. Dille, S. Abrahamsson, and U. Wong, "Miniature 3D microscope and reflectometer for space exploration," in *Proc. IEEE Int. Conf. Comput. Photogr. (ICCP)*, May 2019, pp. 1–8.

[41] *Optical Measurement and Microtopographies—Calibration of Interference Microscopes and Depth Measurement Standards for Roughness Measurement, VDI/VDE-Gesellschaft Mess-und Automatisierungstechnik Standard*, Standard VDI/VDE 2655 Blatt 1.1, Mar. 2008.

[42] (2021). *Edmund Optics USAF Resolution Target Pocket Size (38–710)*. [Online]. Available: https://www.edmundoptics.com/p/usaf-resolution-target-pocket-size/4389

[43] L. Ginner and L. Traxler, "Experimental comparison of optical inline 3D measurement and inspection systems," AIT Austrian Inst. Technol., Vienna, Austria, IEEE Dataport, Dec. 2020, doi: 10.21227/j9x0-g074.

[44] (2020). *Cloudcompare (Version 2.12) [GPL Software]*. [Online]. Available: http://www.cloudcompare.org/

[45] T. Scheimpflug, "Improved method and apparatus for the systematic alteration or distortion of plane pictures and images by means of lenses and mirrors for photography and for other purposes," GB Patent 190 401 196 A, Jan. 1904.

LUKAS TRAXLER received the master's degree in biomedical engineering and the Ph.D. degree in technical physics from the Technical University of Vienna, Austria, in 2014 and 2018, respectively. In 2017, he joined the Center for Vision, Automation & Control, AIT Austrian Institute of Technology, as a Scientist. Since 2014, he has been a Lecturer with the University of Applied Sciences Technikum Wien. His main research interests include technical optics and computational imaging. He received the title Fachhochschulprofessor (FH-Prof.) from the University of Applied Sciences Technikum Wien in 2019.

LAURIN GINNER received the master's degree in physical energy and measurement engineering from the Technical University of Vienna and the Ph.D. degree from the Medical University of Vienna, in 2019. His Ph.D. Thesis was Advanced Techniques for Functional Parallel Optical Coherence Tomography. Since March 2020, he has been with the AIT Austrian Institute of Technology, as a Scientist, working on technical optics and computational imaging. In 2019, he received the Award of Excellence for the 40 best dissertations in Austria, for his Ph.D. thesis.

SIMON BREUSS received the master's degree in computer science from the Alpen-Adria University of Klagenfurt, in 2008. He worked as a member of the System Security Research Group, Alpen-Adria University of Klagenfurt. In 2009, he joined the AIT Austrian Institute of Technology. He is currently working in the field of computational imaging and 3D reconstruction, and is focused on the development and implementation of algorithms, models, and their simulation.

BERNHARD BLASCHITZ received the master's degree in mathematics from the University of Vienna, in 2008, and the Ph.D. degree in applied geometry from the Technical University of Vienna, Austria, in 2014. In 2015, he joined the AIT Austrian Institute of Technology, where he currenty works as a Scientist with the Center for Vision, Automation & Control. He has authored numerous articles and holds two patents related to multi line scan cameras. His main research interests include computational imaging and calibration methods.